IEEE Robotics and Automation Letters (RA-L) paper, presented at ICRA 2026, Vienna, Austria. Cite as RA-L paper.

Filament Sliding Linear Potentiometer-Based Data Glove (FLiPo) for Precisely Annotating Human Finger Poses

Zhisheng Xia, Haochen Yong, Qilong Liu, Zhenghao Ke, Han Ding, and Zhigang Wu, *Member, IEEE*

***Abstract*—Data gloves offer excellent portability and a strong ability to handle occluded movements, making them more advantageous over other methods for capturing complex hand motions in unstructured environments. However, the majority of existing hand-motion-capture gloves do not preserve visual features of the hand, which critically hinders their applicability for automatic pose annotation in RGB images. Here, we propose a data glove based on filament-sliding linear potentiometers (FLiPo), which can maintain finger appearance and ensure high accuracy as well as robustness, paving the way for automatic annotation. In FLiPo, fine filaments (Φ 0.1 mm) are deployed on finger skin to transmit joint arc length variations as well as preserve the hand's visual features, while linear potentiometers used to capture filament length changes are positioned on the arm. Simultaneously, a quantitative occlusion scoring metric is proposed to evaluate the degree of finger occlusion caused by the device. Further, we experimentally analyze the nonlinearities induced by biaxial joint coupling and skin tissue artifact (STA)-related hysteresis, and employ a fully connected neural network to map arc length to joint angles with an MAE of joint angles of 2.15°. Meanwhile, tests under challenging environmental conditions, including heat, moisture, and magnetic interference, are conducted to evaluate its stability. Finally, the system's capability for real-time pose capture with high accuracy, robustness, and low occlusion was demonstrated.**

***Index Terms*—Gesture, posture and facial expressions, wearable robotics, human-centered robotics.**

I. Introduction

IN RECENT years, vision-driven hand tracking methods have been rapidly advancing; however, the methodologies are still severely constrained by the lack of effective methods for annotating large-scale, real-world datasets [1], [2]. Preserving the original visual features during annotation is crucial, as visual markers [3], hand occlusion [4], and texture variations [5] can significantly degrade the accuracy and robustness of the model. Nevertheless, most existing motion capture systems largely overlook the preservation of visual features of the hand during data collection. Furthermore, though contactless annotation techniques such as optical motion capture and point cloud reconstruction help mitigate visual occlusion, they remain ineffective in accurately capturing occluded hand poses, especially during hand-object interactions. By contrast, contact-based methods such as data gloves offer stable and comprehensive capture of diverse hand postures.

Lee et al. [6] proposed a visual-inertial hand motion tracking glove that demonstrates robustness against occlusion, interference, and contact. Park et al. [7] introduced a stretchable glove capable of accurate and robust hand pose reconstruction based on comprehensive motion data. Hughes et al. [8] developed a simple yet inexpensive wearable glove that enables accurate hand pose reconstruction. Park et al. [9] proposed a hand motion capture glove based on a linear potentiometer that can precisely measure finger flexion movement. However, all these designs fully occlude the hand during use. Other hand motion tracking gloves [10], [11], [12], [13], [14], [15] also cause significant occlusion of the fingers.

Meanwhile, Kim et al. [16] proposed a glove based on a substrate-less nanomesh receptor, featuring an ultra-thin and half-transparent layer on the fingers. Tan et al. [17] and Moin et al. [18] introduced gloves based on electromyography (EMG) independently, which leave the fingers completely unobstructed. Although the aforementioned techniques are capable of preserving finger visual features, due to the limitations of their measurement approach, these gloves primarily focus on accurate classification of hand gestures rather than precise regression of joint angles.

To address such a dilemma, a filament sliding linear potentiometer-based data glove (FLiPo) is proposed, as illustrated in Fig. 1. Fine filaments (with a caliber of 0.1 mm) are deployed on the fingers to minimize visual occlusion and ensure accurate and reliable capture of joint movements from all fingers. Technically, one end of the filament is fixed to the phalange across the joints, and the other is connected through a conduit to a linear potentiometer arranged on the arm. Such a measure ensures that there is virtually no occlusion on the skin of the fingers. Then, we built a human hand skeleton model containing 20 joint degrees of freedom and analyzed the linear relationship between single-freedom joint rotation angle and arc length variation, as well as the nonlinear relationship due to multi-freedom joint coupling and skin tissue artifacts (STA). Further, the mapping relationship between finger joint arc length

Received 29 May 2025; accepted 10 December 2025. Date of publication 17 December 2025; date of current version 26 December 2025. This article was recommended for publication by Associate Editor Z. Guo and Editor H. Yu upon evaluation of the reviewers' comments. This work was supported in part by the National Natural Science Foundation of China under Grant 52188102 and 52575018 and in part by the National Key Research and Development Program of China under Grant 2024YFB4707902. *(Corresponding author: Zhigang Wu.)*

Zhisheng Xia, Haochen Yong, Qilong Liu, Zhenghao Ke, Han Ding, and Zhigang Wu are with the State Key Laboratory of Intelligent Manufacturing Equipment, Huazhong University of Science and Technology, Wuhan 430074, China, and also with the Research Center for Intelligent Fibre Devices and Equipment and Technology, and the Shenzhen Loop Area Institute, Wuhan 430074, China (e-mail: xzs@hust.edu.cn; hcyong@hust.edu.cn; lql0827@hust.edu.cn; zhke1037@hust.edu.cn; dinghan@hust.edu.cn; zgwu@hust.edu.cn).

This article has supplementary downloadable material available at https://doi.org/10.1109/LRA.2025.3645653, provided by the authors.

Digital Object Identifier 10.1109/LRA.2025.3645653

IEEE Robotics and Automation Letters (RA-L) paper, presented at ICRA 2026, Vienna, Austria. Cite as RA-L paper.

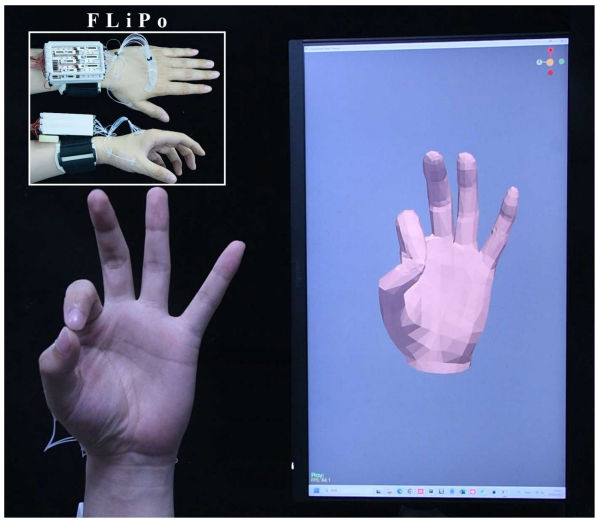

Fig. 1. Demonstration of the FLiPo's hand pose reconstruction capability and the practical wearing configuration on a subject.

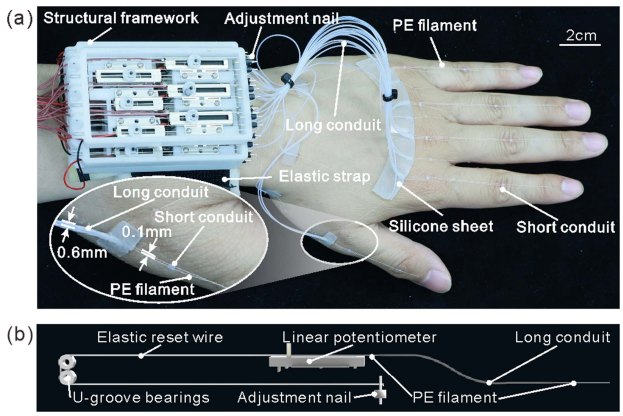

Fig. 2. Assembly diagram and mechanical structure of the FLiPo. (a) Assembly diagram of FLiPo on a human hand. (b) Core mechanical components for measuring the arc length of finger joints.

and angle was established using a fully connected layer network (FCNN). Finally, we achieved an angular estimation of hand motion with a mean absolute error of 2.15°.

The remaining letter is organized as follows. Section II describes the design and working principle of the FLiPo, and demonstrates its stability in sensing. Section III presents the modeling of human hand joints, characterization of the motion of the hand using the FLiPo, and architecture of the mapping network (FCNN). Section IV demonstrates the performance of FLiPo in estimating joint angles. Section V concludes the study and discusses possible future work.

II. Sensor Principles and Design

As illustrated in Fig. 2, the FLiPo consists primarily of linear potentiometers, polyethylene (PE) filaments, elastic reset wires, conduits, U-groove bearings, adjustment nails, elastic straps, silicone sheets, and structural frameworks.

To reliably measure the arc length of human finger joints while preserving visual features, PE filaments (Φ 0.1 mm) are used, with one end attached to a linear potentiometer and the other fixed to finger skin using a medical fast-setting adhesive (2-Octyl cyanoacrylate), as shown in Fig. 2(a). The PE filaments are routed through long conduits from the linear potentiometers on the forearm to the silicone sheet on the back of the hand. Then the silicone sheet is attached to the back of the hand using an alcohol glue (Ben Nye makeup adhesive). This configuration allows the linear potentiometer to be mounted on the arm. Notably, according to the Euler–Bernoulli beam theory, the length of the neutral axis remains unchanged during bending. Due to the buckling behavior of slender rods under compression, rods with a high slenderness ratio experience negligible axial force. Hence, the PE filament enclosed within the long conduit can maintain an almost constant length regardless of wrist movement. Notably, in practice, Teflon conduits are typically difficult to adhere to other materials using glue, but enhancing their surface roughness improves adhesion to the structural framework, silicone sheet, and skin. The adhesive used to attach the PE filaments and short conduits to the skin is a medical fast-setting adhesive (2-Octyl cyanoacrylate).

It is known that linear potentiometers can stably and linearly sense changes in resistance ratios from position information without the need for introducing an extra reference device to eliminate parasitic influences from stimuli, e.g., temperature, magnetic interference [19], [20]. Meanwhile, the joint movement of the hand directly leads to a change in the joint arc length. Therefore, it is feasible to utilize the linear potentiometer slid by filament to sense finger joint movements. More importantly, the linearity of potentiometers makes the data mapping process simpler and more interpretable.

Due to the introduction of the wire-driven mechanism that transmits tension but not thrust, the linear potentiometer cannot move when the finger extends. To tackle this issue, an elastic wire (spandex) is employed to reset the linear potentiometer, and a tension adjustment nail is incorporated, as illustrated in Fig. 2(b). In this scheme, the maximum tension on the PE filaments is equal to the sum of the maximum tension of the elastic reset wire and the friction between the sliding potentiometers and the PE filaments. The minimum tension of the elastic reset wire needs to be slightly greater than the friction to ensure the reset of the linear potentiometer. The maximum tension of the elastic reset wire will increase on the basis of its minimum tension as the linear potentiometer moves away from the initial position. To reduce the maximum tension of the elastic reset wire, the wire is routed around U-groove bearings, Fig. 2(b). By ensuring that the original length of the elastic reset wire far exceeds the stroke variation, it significantly reduces the maximum tension. The maximum sliding tension on the PE filament was measured to be less than 0.16 N using a force gauge, and the average rebound time over the full stroke was 24.38 ms.

For a FLiPo practically working on a hand, a total of 22 such components are integrated into a three-layer structural frame. The layers are fixed with nails, while the elastic straps are attached to the bottom layer using Velcro fasteners.

As illustrated in Fig. 2, to guide motion transmission and minimize the pressure exerted by the filaments on the fingers, PE filaments extended via long conduits to the dorsal side of the hand pass through short conduits (Φ 0.6 mm and 1.5 mm in length) located at each finger joint, and are ultimately fixed onto each phalanx segment. The short conduits can reduce the pressure of the filaments on the joints to 0.173 MPa, while the pressure over 3.183 MPa can pierce the skin [21]. The 0.1 mm diameter PE filaments and the 0.6 mm diameter short conduits on the fingers are nearly invisible, which is crucial for computer vision-based hand gesture recognition [2].

IEEE Robotics and Automation Letters (RA-L) paper, presented at ICRA 2026, Vienna, Austria. Cite as RA-L paper.

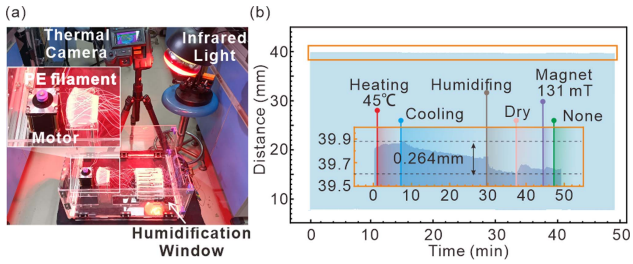

Fig. 3 Sensor anti-interference stability test. (a) Physical diagram of the experimental platform. Infrared light for heating, a humidifying window for humidity control, a switchable top cover for magnet placement, a thermal camera for temperature recording, and a stepper motor for driving cyclic PE filament motion. (b) Data diagram of FLiPo under extreme temperature, humidity, and magnetic field changes. The orange zoom-in shows the variation at the vertical axis maximum caused by environmental changes, with the colored vertical lines indicating changes in environmental parameters.

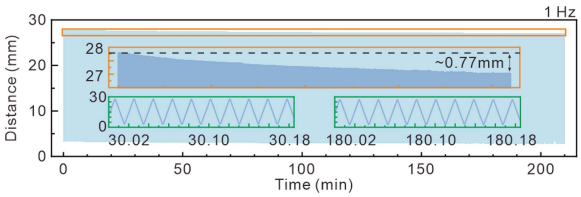

Fig. 4. Sensor repeatability test. Data diagram of FLiPo under 210 minutes of cyclic stretching. The orange zoom-in shows the shift of the vertical axis maximum caused by long-term cyclic stretching. The two green zoom-ins show the actual sensor waveforms at 30 min and 180 min.

The base material of FLiPo is silicone, and the adhesives are commercial cosmetic and medical fast-setting glues, both exhibiting good skin compatibility. Owing to its low skin coverage, FLiPo maintains overall breathability well. Moreover, the mass of FLiPo on the palm is only 3.60 g and 121.37 g on the forearm, imposing a relatively low burden on the hand.

The linear potentiometers are RDC10 series from Alps Alpine, Japan, offering a linearity of ±0.5% . These potentiometers provide highly stable positional feedback as they rely on the ratio of resistances rather than absolute resistance values. It makes them unaffected by the variation from temperature, humidity, and magnetic interference. As the filaments transmit motion via the aforementioned mechanism, the linear potentiometers' stability data alone cannot fully represent the overall sensor stability of the FLiPo. Therefore, we conducted sensor stability tests under varying conditions of temperature, humidity, and magnetic interference.

As illustrated in Fig. 3(a), within a semi-enclosed transparent box, the FLiPo was subjected to the tension of the PE filaments extending from the silicone sheet, driven by the rotation of a stepper motor. The temperature inside the box was adjusted using infrared light, the humidity was controlled by spraying water mist from the humidification window, and the magnetic field strength was varied by adjusting the position of a magnet. As illustrated in Fig. 3(b), the cyclic stroke of the sensor is 35 mm within a total travel range of 47 mm, and the variation in sensor readings under different stimuli is 0.264 mm, resulting in an environmental impact on the sensor of only 7.54‰. This demonstrates that the FLiPo exhibits excellent stability concerning temperature, humidity, and magnetic field variations. As shown in Fig. 4, the cyclic stroke of the sensor is 23.8 mm within the total travel range of 32 mm. After 12,600 cycles, the sensor's overall travel range shifts downward, but this shift accounts for only 3.24% of the total range of motion. That is, the data curves in Figs. 3 and 4 indicate that, even under extreme environmental conditions and prolonged operation, the FLiPo maintains high stability.

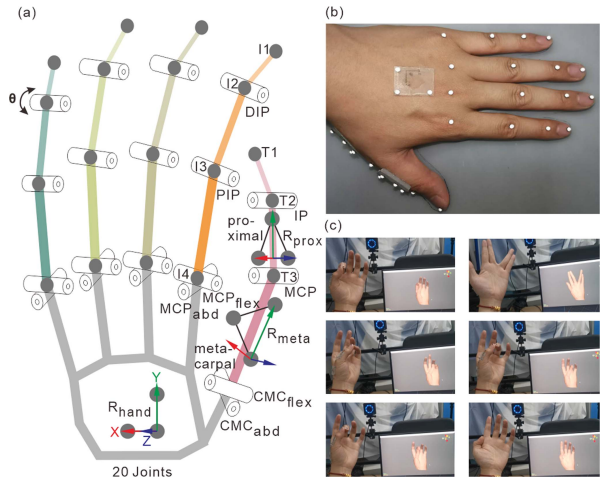

Fig. 5 Reconstruction of the hand model and visualization of the resulting hand poses. (a) Illustration of the Forward Kinematics (FK) hand model used to reconstruct hand pose based on joint angles, (b) Illustration of the hand zero pose and placement of optical markers for motion capture, and (c) Comparison between actual hand poses and reconstructed poses.

III. Theoretical Modeling and Formulations

In this section, we first introduce the forward kinematics (FK) model adopted for the hand and explain how the model parameters are derived from motion capture marker data. Then, we will explain how the relationship between joint angle and joint arc length is interpreted as a combination of linear principal components and nonlinear effects through theoretical modeling. Finally, we used a simple, fully connected neural network to model the relationship between joint angle and joint arc length.

A. Construction of the Forward Kinematics (FK) Hand Model

As illustrated in Fig. 5(a), based on the FK model of Park et al. [7], we developed an improved version to address issues encountered in our experiments. Specifically, we observed that it is difficult to ensure the precise placement of the rigid marker body placed on the metacarpal bone and proximal phalanx of the thumb owing to STA. Meanwhile, as noted by Bullock et al. [22], the relative motion between the metacarpal bone and the proximal phalanx of the thumb does not occur about a single, well-defined axis. In the original FK model, only two rotation parameters (α and γ) were used to describe the orientation of the carpometacarpal (CMC) joint and metacarpophalangeal (MCP) joint base frames relative to their respective parent joint frames. To enhance model robustness and precision, we introduce four rotation matrices to represent both the misalignment caused by marker attachment on the two thumb segments and the orientation of the CMC and MCP reference coordinate systems relative to their respective parent coordinate system.

Following the approach of Park et al. [7], we model the thumb's interphalangeal (IP) joint and MCP joints, as well as the proximal interphalangeal (PIP) joints and distal interphalangeal (DIP) joints of the rest four fingers, as flexion joints with one degree of freedom (DoF). In contrast, the thumb's CMC joint

IEEE Robotics and Automation Letters (RA-L) paper, presented at ICRA 2026, Vienna, Austria. Cite as RA-L paper.

and the MCP joints of the other fingers are modeled with two DoFs, including both flexion and abduction movements.

As illustrated in Fig. 5(b), in the zero pose, all five fingers lie within the XY-plane of the palm pose matrix $\boldsymbol{R}_{\mathrm{hand}}$. The thumb is extended and forms a 45° angle with the Y-axis of $\boldsymbol{R}_{\mathrm{hand}}$, while the other four fingers are extended and aligned parallel to the Y-axis. Taking the index finger as an example, in the zero pose, the abduction (abd) axis of the proximal phalanx aligns with the Z-axis of $\boldsymbol{R}_{\mathrm{hand}}$, and its flexion (flex) axis aligns with the X-axis; the flexion axes of the middle and distal phalanges also align with the X-axis of $\boldsymbol{R}_{\mathrm{hand}}$. The θ_{MCPabd}, $\theta_{\mathrm{MCPflex}}$, θ_{PIP}, and θ_{DIP} represent the rotation angles around the four aforementioned axes of the index finger. As illustrated in Fig. 5(a), I_1, I_2, I_3, and I_4 denote the corresponding joint points of the index finger, and $\boldsymbol{V}_{\mathrm{Iij}}$ represents the vector from joint I_i to joint I_j, where i and j are the joint indices from 1 to 4. Similarly, the thumb vectors are denoted as $\boldsymbol{V}_{\mathrm{Tij}}$. The angles are calculated as follows,

$$\begin{bmatrix}\theta_{\mathrm{MCPabd}}\\ \theta_{\mathrm{MCPflex}}\\ \theta_{\mathrm{PIP}}\\ \theta_{\mathrm{DIP}}\end{bmatrix} = \begin{bmatrix}\arctan2\left(\frac{[1\ \ 0\ \ 0]^T\cdot \boldsymbol{R}_{\mathrm{hand}}^T\cdot \boldsymbol{V}_{\mathrm{I43}}}{[0\ \ 1\ \ 0]^T\cdot \boldsymbol{R}_{\mathrm{hand}}^T\cdot \boldsymbol{V}_{\mathrm{I43}}}\right)\\ \arcsin\left(\frac{[0\ \ 0\ \ 1]^T\cdot \boldsymbol{R}_{\mathrm{hand}}^T\cdot \boldsymbol{V}_{\mathrm{I43}}}{\left\|\boldsymbol{R}_{\mathrm{hand}}^T\cdot \boldsymbol{V}_{\mathrm{I43}}\right\|}\right)\\ \arccos((\boldsymbol{V}_{\mathrm{I43}}\cdot\boldsymbol{V}_{\mathrm{I32}})/(\|\boldsymbol{V}_{\mathrm{I43}}\|\cdot\|\boldsymbol{V}_{\mathrm{I32}}\|))\\ \arccos((\boldsymbol{V}_{\mathrm{I32}}\cdot\boldsymbol{V}_{\mathrm{I21}})/(\|\boldsymbol{V}_{\mathrm{I32}}\|\cdot\|\boldsymbol{V}_{\mathrm{I21}}\|))\end{bmatrix}. \tag{1}$$

However, due to the anatomical complexity of the thumb, its joint axes cannot be easily defined, and such misalignments vary across individuals. In our model, this variability is addressed through parameterization using four rotation matrices: $\boldsymbol{R}_{\mathrm{m1}}$ denotes an offset matrix from the measured palm coordinate frame $\boldsymbol{R}^*{}_{\mathrm{hand}}$ to the zero-pose anatomical metacarpal bone pose $\boldsymbol{R}_{\mathrm{meta0}}$; $\boldsymbol{R}_{\mathrm{m2}}$ denotes an offset matrix from measured metacarpal bone pose $\boldsymbol{R}^*{}_{\mathrm{meta}}$ to the anatomical metacarpal bone pose $\boldsymbol{R}_{\mathrm{meta}}$ (the variation in rigid body attachment positions on the skin); $\boldsymbol{R}_{\mathrm{p1}}$ denotes an offset matrix from $\boldsymbol{R}^*{}_{\mathrm{meta}}$ to the zero-pose anatomical proximal phalanx pose $\boldsymbol{R}_{\mathrm{prox0}}$; and $\boldsymbol{R}_{\mathrm{p2}}$ denotes an offset matrix from measured proximal phalanx pose $\boldsymbol{R}^*{}_{\mathrm{prox}}$ to the anatomical proximal phalanx pose $\boldsymbol{R}_{\mathrm{prox}}$. θ_{CMCabd}, $\theta_{\mathrm{CMCflex}}$, θ_{MCP}, and θ_{IP} is the same as those used for the index finger. The four rotation matrices and angles are calculated as follows:

$$\begin{aligned}\boldsymbol{R}_{CMC} &= [\boldsymbol{R}^*_{hand}\cdot\boldsymbol{R}_{m1}]^T\cdot\boldsymbol{R}^*_{meta}\cdot\boldsymbol{R}_{m2}\\ &= \boldsymbol{R}^T_{meta0}\cdot\boldsymbol{R}_{meta} = \boldsymbol{R}_{\mathrm{CMC}x}\cdot\boldsymbol{R}_{\mathrm{CMC}y}\cdot\boldsymbol{R}_{\mathrm{CMC}z},\end{aligned} \tag{2}$$

$$\begin{aligned}\boldsymbol{R}_{MCP} &= \left[\boldsymbol{R}^*_{meta}\cdot\boldsymbol{R}^*_{p1}\right]^T\cdot\boldsymbol{R}^*_{prox}\cdot\boldsymbol{R}^*_{p2}\\ &= \boldsymbol{R}^T_{prox0}\cdot\boldsymbol{R}_{prox} = \boldsymbol{R}_{\mathrm{MCP}x}\cdot\boldsymbol{R}_{MCPy}\cdot\boldsymbol{R}_{MCPz},\end{aligned} \tag{3}$$

$$\boldsymbol{R}_{CMC} = \boldsymbol{R}_{CMCabd}(\theta_{CMCabd})\cdot\boldsymbol{R}_{\varepsilon 1}\cdot\boldsymbol{R}_{CMCflex}(\theta_{CMCflex}), \tag{4}$$

$$\boldsymbol{R}_{MCP} = \boldsymbol{R}_{MCP}(\theta_{MCP})\cdot\boldsymbol{R}_{\varepsilon 2}\cdot\boldsymbol{R}_{\varepsilon 3}, \tag{5}$$

$$\theta_{IP} = \arccos((\boldsymbol{V}_{T32}\cdot\boldsymbol{V}_{T21})/(\|\boldsymbol{V}_{T32}\|\cdot\|\boldsymbol{V}_{T21}\|)). \tag{6}$$

The matrices $\boldsymbol{R}_{\mathrm{CMC}}$ and $\boldsymbol{R}_{\mathrm{MCP}}$ represent the pre-optimized rotation matrices and corresponding XYZ Euler angles ($\boldsymbol{R}_{\cdot\mathrm{x}}$, $\boldsymbol{R}_{\cdot\mathrm{y}}$, and $\boldsymbol{R}_{\cdot\mathrm{z}}$, where "·" denotes the CMC and MCP joints.) of the thumb joints. According to anatomical constraints, the optimization objective is to make $\boldsymbol{R}_{\mathrm{CMCy}}$, $\boldsymbol{R}_{\mathrm{MCPy}}$, and $\boldsymbol{R}_{\mathrm{MCPz}}$ approximate identity matrices. After optimization, the anatomically

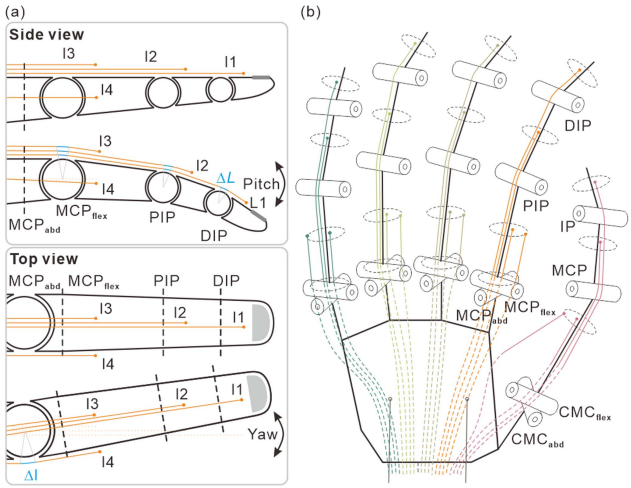

Fig. 6. Modeling diagram of the FLiPo measuring principle. (a) Schematic diagram of the linear measurement principle for index finger joint angles and (b) Layout and coordinate axes setup for all fingers.

constrained rotation matrices $\boldsymbol{R}_{\mathrm{CMC}}$ and $\boldsymbol{R}_{\mathrm{MCP}}$ are obtained. Euler angle decomposition of these matrices yields θ_{CMCabd}, $\theta_{\mathrm{CMCflex}}$, θ_{MCP}, along with three residual rotation matrices $\mathrm{R}_{\varepsilon\mathrm{i}}$ (i = 1,2,3), which are approximately identity matrices. The angle θ_{IP} is calculated using the same approach as for θ_{PIP} and θ_{DIP}. As shown in Fig. 5(c), after applying the aforementioned parameter optimizations, the FK hand model can accurately reconstruct hand motions.

Further, we compared our method with that of Park et al [7]. In our approach, if the $\boldsymbol{R}_{\mathrm{m1}}$ matrices is set to a rotation around the Z-axis and the $\boldsymbol{R}_{\mathrm{m2}}$ matrix is set to the identity matrix, the method becomes equivalent to the optimization approach in [7]. The constraint settings of these two matrices are treated as Constraint 1 and Constraint 2. The mean absolute error (MAE) of $\mathrm{R}_{\varepsilon 1}$ in axis–angle representation is 2.56° without constraints, 2.73° with Constraint 1, 2.88° with Constraint 2, and 3.09° when both constraints are applied. These results hint at an improvement of our method over the approach in [7].

B. Sensing Principle of FLiPo

As illustrated in Fig. 6(a), in the side view of the index finger, l_1, l_2, and l_3 are fixed along the midlines of the proximal phalanx, middle phalanx, and distal phalanx, respectively. These lines measure the arc length changes resulting from the rotations of the $\mathrm{MCP}_{\mathrm{flex}}$, PIP, and DIP joints. In the top view, l_4 is fixed on the midline of the side surface of the phalanx proximal manus, which can measure the arc length changes caused by the rotation of the $\mathrm{MCP}_{\mathrm{abd}}$ joint. Under this revolute joint model, the arc length and the angle are linearly related, meaning that the joint angles are transmitted via the line lengths outside the fingers. The same principle applies to the other four fingers. The linear relationship between joint angle θ and arc length $\boldsymbol{l}$ is given by the following expression, where r is the rotation radius of each joint, similar to the previous work [9],

$$\begin{bmatrix}\Delta\theta_{MCP(CMC)abd}\\ \Delta\theta_{MCP(CMC)flex}\\ \Delta\theta_{PIP}\\ \Delta\theta_{DIP}\end{bmatrix} = \begin{bmatrix}\Delta l_3/r_{MCP(CMC)abd}\\ \Delta l_4/r_{MCP(CMC)flex}\\ (\Delta l_2-\Delta l_3)/r_{PIP}\\ (\Delta l_1-\Delta l_2)/r_{DIP}\end{bmatrix}. \tag{7}$$

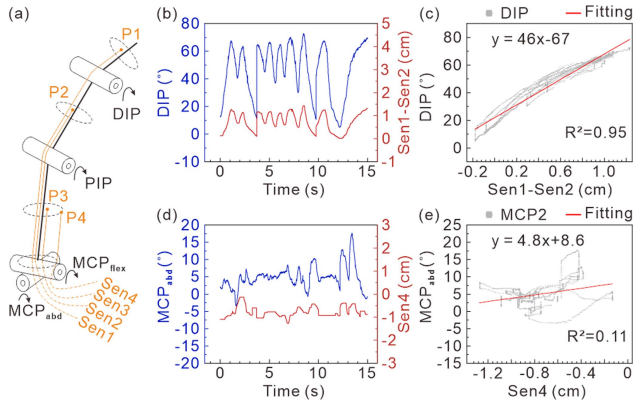

Fig. 7. Relationship between the $\mathrm{MCP_{abd}}$ joint and DIP joint angles of the index finger and the length of the PE filaments.

However, due to the distribution of quite a few muscles in the palm, l_4 cannot be positioned along the midline of the side surface of the proximal phalanx. Especially for the thumb, its l_4 can only be extended laterally to the back of the hand, as shown in Fig. 6(b). Consequently, l_4 actually reflects the rotational information of both the $\mathrm{MCP_{abd}}$ and $\mathrm{MCP_{flex}}$ joints. Moreover, the STA of the hands caused the relative movement among the fixed points of the lines and the finger bones. It can lead to mutual interference on the lengths of the lines between the five fingers and may even result in the shifting of the silicone sheet.

To address these nonlinear effects, we added two additional lines on the back of the hand, as shown in Fig. 6(b), to measure the displacement of the silicone sheet. Moreover, we utilized a simple, fully connected neural network (FCNN) to obtain a nonlinear mapping $\boldsymbol{l}$to θ. The FCNN takes the lengths of all 22 lines as input and outputs a 20-dimensional Euler angle representation through six hidden layers. The hidden layers consist of fully connected neurons with dimensions of 64, 256, 512, 1024, 512, and 128, respectively. The ELU activation function is applied to the first two layers, while the remaining layers use the ReLU activation function. The network formula is as follows,

$$\boldsymbol{h}^{(i)} = \boldsymbol{f}\left(\boldsymbol{W}^{(i)}\boldsymbol{h}^{(i-1)} + \boldsymbol{b}^{(i)}\right)_{i=1,2\ldots,6}, \boldsymbol{h}^{(0)} = \boldsymbol{l}, \quad (8)$$

$$\boldsymbol{\theta} = \boldsymbol{W}^{(I)}\boldsymbol{h}^{(I-1)} + \boldsymbol{b}^{(I)}, \boldsymbol{I} = 7, \quad (9)$$

$$\mathrm{L} = \frac{1}{N}\sum_{j=1}^{N}\left|\boldsymbol{\theta}_j - \widehat{\boldsymbol{\theta}}_j\right|, N = 640, \quad (10)$$

where $\boldsymbol{h}$ represents the hidden layer outputs, $\boldsymbol{l}$ is the 22-dimensional input vector of line lengths, θ is the 20-dimensional output vector of joint angles, f is the activation function between layers, $\boldsymbol{L}$ is the L1 loss function, and N is the batch size (set to 640). In total, the network comprises 1,267,924 parameters, yielding a lightweight model of only 4.88 MB.

As illustrated in Fig. 7, we experimented to verify the relationship between the length of the PE filaments and the index finger joint angles. As shown in Fig. 7(b)–(c), it can be seen that the DIP angle of the index finger is shown to be linearly related to the change of joint arc length (equal to the difference between Sensor1 and Sensor2) with an R^2 of 0.95. The result indicates that the joint arc Δl is linearly related to the change in joint angle $\Delta\theta$. However, as for the MCP angle, the angle value is no longer linearly related to the joint arc length (value of Sensor4), as shown in Fig. 7(d)–(e). It's because the MCP joints of the index fingers have two coupled rotational freedoms and STA. The same non-linear behavior is observed in the CMC joint of the thumb and the MCP joints of the other fingers. This result is consistent with our earlier theoretical analysis and strongly supports the validity of our theoretical approach.

IV. Experimental

To evaluate the accuracy of the FLiPo, we conducted both data collection experiments, as shown in Fig. 8, and real-time demonstration experiments, as shown in Fig. 9(as well as an attached supporting video 1). The real-time demonstrations include the Kapandji test [23], digit gesture recognition, and object manipulation tasks. Compared to previous works, our FLiPo exhibited excellent measurement accuracy. Demonstration videos are provided, where the virtual hand was only rendered at 30 FPS due to graphical load, while the glove's sampling rate is able to reach up to 200 Hz.

A. Experimental Setup

In the optical motion capture (opt-mocap) room, both the data collection system and the opt-mocap system (FZMotion Mocap System) were activated simultaneously at a sampling frequency of 200 Hz. The thumb sequentially performs joint movements across its full range of motion three times in the order of CMC abduction, CMC flexion, MCP, and IP. The same protocol is applied to the other four fingers. After completing two full cycles, all fingers execute random motions, followed by commonly predefined gestures such as numerical hand signs. This sequence constitutes a complete data collection session, with each session containing approximately 40,000 frames of data (about 200 seconds). The data was then processed using a desktop computer with an NVIDIA 2060 GPU for training and finger pose estimation. In total, 1 million frames were collected, from which 920,000 frames were used as the training set and 80,000 frames as the test set.

B. Results Analysis

In Table I, by observing the MAE and RMSE, the results show that the MAE and RMSE of the thumb CMC joint and the MCP joints of the other four fingers are only slightly higher than those of the PIP and DIP joints. This observation aligns with our analysis of the nonlinear relationship caused by multi-degree-of-freedom joint coupling and skin tissue artifacts (STA), and it also demonstrates the effectiveness of the FCNN-based mapping method. A significant improvement in accuracy was specified compared with commercial bend sensors (5° for single-freedom joints) and clinical measuring strategy- goniometer (5° for all joints) [24]. By observing the angle ranges, the results indicate that the collected data sufficiently reflect the motion space of each finger joint, even including backward bending of the fingers.

In Table II, we compare our method with other representative glove-based hand motion capture methods in terms of accuracy, finger occlusion, and sampling frequency. Accuracy is measured using the Mean Absolute Error (MAE), while finger occlusion is evaluated using a proposed scoring mechanism. Specifically, each finger is divided into phalanx segments, and for each segment. Segment score 1 point if less than 5% of

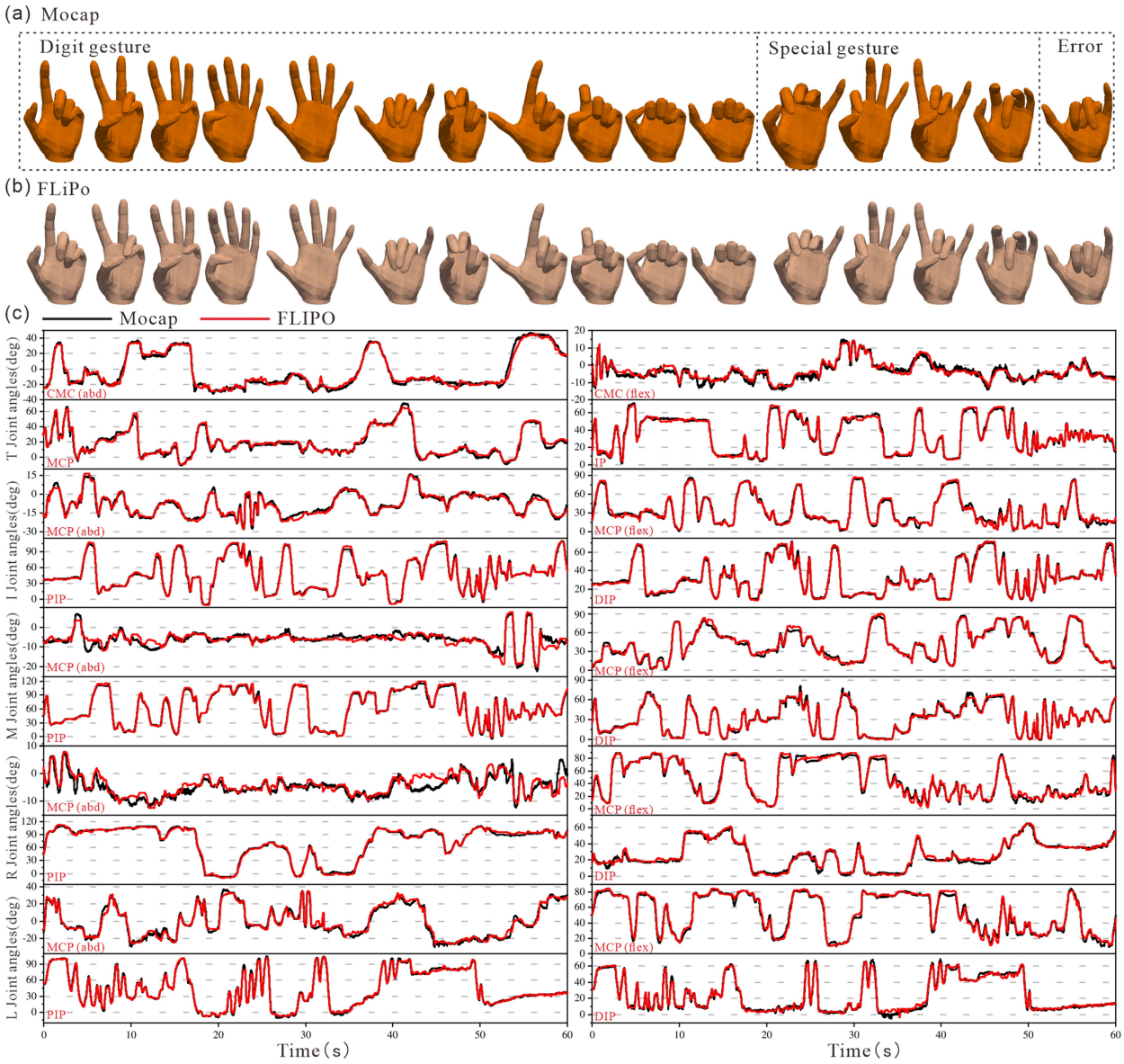

Fig. 8. Real-time estimation of joint angles for all fingers. (a) Hand poses reconstructed from optical motion capture in the test set. (b) Hand poses estimated by the FLiPo system in the test set. (c) Plot of the time trajectories of the estimated and true joint angles. T, Thumb; I, Index; M, Middle; R, Ring; L, Little.

their surface area is occluded in 90% of viewing directions, 0.5 points if 5–50% is occluded in 90% of viewing directions, and 0 points for other. The occlusion score is calculated by summing the scores of the finger segments actually measured by the glove and dividing by the number of segments included in the evaluation. The score ranges from 0 to 1, with values closer to 1 indicating better preservation of finger visual features. Our method reaches the current research standard in joint angle estimation accuracy and sampling frequency. In particular, it significantly outperforms existing approaches in occlusion scoring.

To demonstrate the estimation characteristics of FLiPo during joint motion, we selected a representative sequence of 12,000 frames and 16 typical gesture frames from the 80,000-frame test dataset and visualized them. Fig. 8(a)–(b) illustrate the 3D reconstructed hand gestures in a virtual environment using motion capture data and FLiPo data, respectively. The gestures shown are representative actions from the test set, serving as a qualitative evaluation of the proposed glove's measurement accuracy. A visual comparison reveals that the estimations made by the FLiPo are nearly indistinguishable from those obtained via motion capture. Notably, while the Mocap reconstruction fails in the final gesture due to marker issues, the FCNN-based FLiPo glove still reproduces the hand motion robustly and accurately. Fig. 8(c) presents the real-time estimated joint angles of each joint across all five fingers, derived from both motion capture data and FLiPo data. The plots display representative temporal sequences of joint motion selected from the test set. In each subplot, the black lines represent the ground-truth data obtained from the motion capture system, while the red lines denote the corresponding estimations made by FLiPo. The close overlap between the FLiPo and motion capture curves across all joints indicates a high level of estimation accuracy achieved by the proposed system.

IEEE Robotics and Automation Letters (RA-L) paper, presented at ICRA 2026, Vienna, Austria. Cite as RA-L paper.

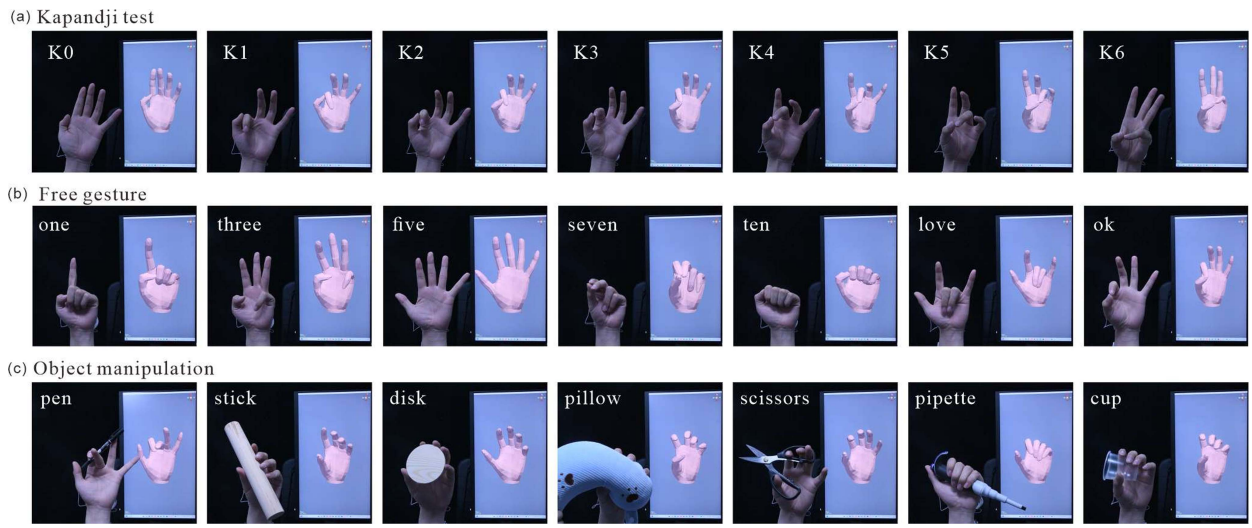

Fig. 9. Real-time comparison of Virtual Motions Estimated by FLiPo and Actual Human Hand Movements. (a) Kapandji test, (b) Free gesture and (c) Object manipulation tasks.

TABLE I
ALL JOINT ANGLE ESTIMATION ERRORS AND MOTION RANGE

Finger Joint		Error (°)		Angle range (°)	
Finger	Joint	MAE	RMSE	Min	Max
Thumb	CMC_{abd}	3.30	4.30	-30.96	45.77
	CMC_{flex}	1.50	2.01	-14.41	17.41
	MCP	2.04	2.67	-9.13	69.48
	DIP	2.17	2.85	-0.85	75.67
Index	MCP_{abd}	1.51	1.98	-29.45	16.37
	MCP_{flex}	2.97	3.83	-7.86	94.42
	PIP	1.87	2.53	-12.42	115.74
	DIP	1.32	1.92	7.07	78.97
Middle	MCP_{abd}	1.20	1.77	-23.82	7.71
	MCP_{flex}	2.86	3.63	-6.30	90.49
	PIP	2.24	2.98	-14.69	120.17
	DIP	1.60	2.22	-3.30	79.28
Ring	MCP_{abd}	1.52	2.30	-12.44	12.71
	MCP_{flex}	3.04	3.89	-3.92	92.72
	PIP	2.24	3.02	-14.46	113.93
	DIP	1.94	2.71	-3.58	70.11
Little	MCP_{abd}	2.62	3.47	-31.19	38.26
	MCP_{flex}	2.63	3.45	2.29	84.83
	PIP	2.50	3.32	-11.10	109.42
	DIP	2.02	2.70	-3.83	67.50

TABLE II
COMPARISON WITH OTHER GLOVE ACCURACY, FINGER OCCLUSION, AND FREQUENCY

Glove	MAE (°)	Occlusion scores[1]	frequency (Hz)
Park et al.[7]	3.91	0 (almost complete occlusion)	60
Hughes et al.[8]	4.78	0 (almost complete occlusion)	16
Michaud et al. [10]	9	0.25 (partial occlusion)	**1000**
Kim et al. [11]	1.63	0.33 (partial occlusion)	/
Tashakori et al. [12]	**1.21**	0 (almost complete occlusion)	20
Fang et al. [13]	/	0.5 (partial occlusion)	/
Glauser et al. [14]	5.30	0 (almost complete occlusion)	60
Pro Fidelity Glove StretchSense [25]	/	0.33 (partial occlusion)	120
Ours (FLiPo)	2.15	**0.97** (almost no occlusion)	200

[1]The occlusion score of 0–0.1 indicates almost complete occlusion, 0.1–0.9 indicates partial occlusion, and 0.9–1 indicates almost no occlusion.

To assess the cross-user robustness of FLiPo, we conducted an additional experiment on a second volunteer characterized by smaller hand dimensions, thinner phalanges, and more severe skin-slip effects. Direct application of the initial model resulted in substantial errors, indicating that user-specific adaptation is necessary. We collected a total of 500,000 frames (440,000 for training and 60,000 for testing), requiring only half the data volume of the first training phase. With a lightweight fine-tuning stage initialized from the pretrained model, FLiPo quickly converged and reached an MAE of 2.45° within four epochs. These results show that, for different users, the system attains high accuracy with only a simplified and lightweight recalibration.

Representative real-time motion capture and 3D visualization results are provided in the supplementary video.

Fig. 9 presents a real-time comparison between virtual hand motions estimated by FLiPo and actual human hand movements. The virtual hand is driven by the previously introduced FK model, with its bone length parameters adjusted to approximate those of the subject. No kinematic constraints were applied during the reconstruction process. The hand motion tasks include the Kapandji test, free gesture, and object manipulation. A demonstration video is provided in the supplementary material for more intuitive visualization.

The reconstructed hand poses closely resemble the actual hand movements and accurately reproduce the full range of DoFs for each finger joint. Notably, the successful reconstruction of the Kapandji contact test—achieved without any kinematic constraints or tactile sensors—strongly highlights the accuracy of the joint angle estimations. The Kapandji score achieved was

IEEE Robotics and Automation Letters (RA-L) paper, presented at ICRA 2026, Vienna, Austria. Cite as RA-L paper.

7, with the missing 4 points corresponding to the contacts of the little finger (excluding the fingertip). These contacts were not achievable as they required significant motion of the little finger's metacarpal bone, which is not modeled for the four fingers in the FK system we used. The free gestures demonstrate the glove's potential for applications such as sign language recognition, while the object manipulation tasks showcase its robustness in scenarios involving soft and hard contact as well as occlusion during hand-object interactions.

Finally, the supplementary video also shows FLiPo's real-time reconstruction under temperature variations, magnetic field variations, and transitions between underwater and above-water environments, further supporting its robustness as validated by the stability tests in the Sensor Principles and Design section.

V. Conclusion

In this work, we propose a filament sliding linear potentiometer-based data glove (FLiPo) for automatically annotating finger poses in RGB images with high accuracy, while preserving the natural visual features of the hand. The design addresses the common issue of severe finger occlusion found in existing contact-based hand motion capture gloves, effectively preserving the visual features of the fingers while addressing the limitations of electromyography (EMG)-based methods, which struggle to accurately estimate joint postures.

As shown in Table II, FLiPo, with its high accuracy, high sampling rate, and minimal finger occlusion, demonstrates greater advantages in hand motion annotation tasks involving dynamic movements. Creating and utilizing datasets annotated by FLiPo will greatly advance the development of vision-driven hand tracking methods.

However, during the experiments, we also identified two limitations of this work. As FLiPo requires gluing parts during assembly, each reattachment or replacement of the user alters the data distribution. This necessitates retraining the FCNN model, which, though negligible for data annotation, limits FLiPo's practicality as a daily-use device. Specialized normalization of glove-collected data, together with adjustments to the network structure, such as long short-term memory (LSTM), may help mitigate this issue. Additionally, the FLiPo currently captures motion data only from the fingers and not the wrist, which is a common limitation in the data gloves field [7]. By relocating the silicone sheet to the forearm and addressing the nonlinear interference introduced by wrist movements in the data mapping process, it may be possible to enable wrist tracking.

Acknowledgment

The authors would like to appreciate FZMotion for their support of the Optical motion capture equipment.

References

[1] G. Garcia-Hernando, S. Yuan, S. Baek, and T.-K. Kim, "First-person hand action benchmark with RGB-D videos and 3D hand pose annotations," in *Proc. IEEE/CVF Conf. Comput. Vis. Pattern Recognit.*, Salt Lake City, UT, USA, Jun. 2018, pp. 409–419.

[2] T. Ohkawa, R. Furuta, and Y. Sato, "Efficient annotation and learning for 3D hand pose estimation: A survey," *Int. J. Comput. Vis.*, vol. 131, no. 12, pp. 3193–3206, Dec. 2023.

[3] J. Rosskamp, R. Weller, and G. Zachmann, "Effects of markers in training datasets on the accuracy of 6D pose estimation," in *Proc. IEEE Winter Conf. Appl. Comput. Vis.*, Waikoloa, HI, USA, Jan. 2024, pp. 4445–4454.

[4] S. Yuan, Q. Ye, B. Stenger, S. Jain, and T.-K. Kim, "BigHand2.2M benchmark: Hand pose dataset and state of the art analysis," in *Proc. IEEE Conf. Comput. Vis. Pattern Recognit.*, Honolulu, HI, USA, Jul. 2017, pp. 2605–2613.

[5] Z. Tu et al., "Consistent 3D hand reconstruction in video via self-supervised learning," *IEEE Trans. Pattern Anal. Mach. Intell.*, vol. 45, no. 8, pp. 9469–9485, Aug. 2023.

[6] Y. Lee, W. Do, H. Yoon, J. Heo, W. Lee, and D. Lee, "Visual-inertial hand motion tracking with robustness against occlusion, interference, and contact," *Sci. Robot.*, vol. 6, no. 58, Sep. 2021, Art. no. eabe1315.

[7] M. Park, T. Park, S. Park, S. J. Yoon, S. H. Koo, and Y.-L. Park, "Stretchable glove for accurate and robust hand pose reconstruction based on comprehensive motion data," *Nature Commun.*, vol. 15, no. 1, Jul. 2024, Art. no. 5821.

[8] J. Hughes, A. Spielberg, M. Chounlakone, G. Chang, W. Matusik, and D. Rus, "A simple, inexpensive, wearable glove with hybrid resistive-pressure sensors for computational sensing, proprioception, and task identification," *Adv. Intell. Syst.*, vol. 2, no. 6, 2020, Art. no. 2000002.

[9] Y. Park, J. Lee, and J. Bae, "Development of a wearable sensing glove for measuring the motion of fingers using linear potentiometers and flexible wires," *IEEE Trans. Ind. Informat.*, vol. 11, no. 1, pp. 198–206, Feb. 2015.

[10] H. O. Michaud, L. Dejace, S. De Mulatier, and S. P. Lacour, "Design and functional evaluation of an epidermal strain sensing system for hand tracking," in *Proc. IEEE Int. Conf. Intell. Robots Syst.*, Daejeon, South Korea, Oct. 2016, pp. 3186–3191.

[11] J. S. Kim et al., "Wearable hand module and real-time tracking algorithms for measuring finger joint angles of different hand sizes with high accuracy using FBG strain sensor," *Sensors*, vol. 20, no. 7, Jan. 2020, Art. no. 1921.

[12] A. Tashakori et al., "Capturing complex hand movements and object interactions using machine learning-powered stretchable smart textile gloves," *Nature Mach. Intell.*, vol. 6, no. 1, pp. 106–118, Jan. 2024.

[13] B. Fang, F. Sun, H. Liu, and D. Guo, "A novel data glove for fingers motion capture using inertial and magnetic measurement units," in *Proc. IEEE Int. Conf. Robot. Biomimetics*, Qingdao, China, Dec. 2016, pp. 2099–2104.

[14] O. Glauser, S. Wu, D. Panozzo, O. Hilliges, and O. Sorkine-Hornung, "Interactive hand pose estimation using a stretch-sensing soft glove," *ACM Trans. Graph.*, vol. 38, no. 4, pp. 41:1–41:15, Jul. 2019.

[15] Y. Su, G. Li, Y. Deng, I. Sarakoglou, N. G. Tsagarakis, and J. Chen, "The joint-space reconstruction of human fingers by using a highly under-actuated exoskeleton," in *Proc. IEEE Int. Conf. Robot. Automat.*, Yokohama, Japan, May 2024, pp. 9645–9651.

[16] K. K. Kim et al., "A substrate-less nanomesh receptor with meta-learning for rapid hand task recognition," *Nature Electron.*, vol. 6, no. 1, pp. 64–75, Jan. 2023.

[17] P. Tan et al., "Self-powered gesture recognition wristband enabled by machine learning for full keyboard and multicommand input," *Adv. Mater.*, vol. 34, no. 21, 2022, Art. no. 2200793.

[18] A. Moin et al., "A wearable biosensing system with in-sensor adaptive machine learning for hand gesture recognition," *Nature Electron.*, vol. 4, no. 1, pp. 54–63, Jan. 2021.

[19] R. R. Kanchi and N. Gosala, "Design and development of an embedded system for testing the potentiometer linearity," *Sensors Transducers*, vol. 112, no. 1, pp. 107–117, Jan. 2010.

[20] M. Papoutsidakis, A. Srivastava, and S. Chowdhary, "Displacement sensors for linear electrical, hydraulic and pneumatic actuators," in *Proc. Amity Int. Conf. Artif. Intell.*, Dubai, United Arab Emirates, Feb. 2019, pp. 269–273.

[21] D. W. Bodhale, A. Nisar, and N. Afzulpurkar, "Design, fabrication and analysis of silicon microneedles for transdermal drug delivery applications," in *Proc. Int. Conf. Develop. Bio. Engineer. Vietnam*, Berlin, Heidelberg, 2010, pp. 84–89.

[22] I. M. Bullock, J. Borràs, and A. M. Dollar, "Assessing assumptions in kinematic hand models: A review," in *Proc. 4th IEEE RAS EMBS Int. Conf. Biomed. Robot. Biomechatronics*, Rome, Italy, Jun. 2012, pp. 139–146.

[23] A. Kapandji, "Clinical test of apposition and counter-apposition of the thumb," *Ann Chir Main*, vol. 5, no. 1, pp. 67–73, Jan. 1986.

[24] S. Lu, D. Chen, C. Liu, Y. Jiang, and M. Wang, "A 3-D finger motion measurement system via soft strain sensors for hand rehabilitation," *Sensors Actuators A: Phys.*, vol. 285, pp. 700–711, Jan. 2019.

[25] StretchSense, "MoCap pro fidelity glove," 2022. Accessed: 2025. [Online]. Available: https://stretchsense.com/mocap-pro-fidelity-glove-2/